Proximity exchange effects in MoSe$_2$ and WSe$_2$ heterostructures with CrI$_3$: Twist angle, layer, and gate dependence

Klaus Zollner ,[*] Paulo E. Faria Junior, and Jaroslav Fabian
Institute for Theoretical Physics, University of Regensburg, 93040 Regensburg, Germany

Proximity effects in two-dimensional (2D) van der Waals heterostructures offer controllable ways to tailor the electronic band structure of adjacent materials. Proximity exchange in particular is important for making materials magnetic without hosting magnetic ions. Such *synthetic* magnets could be used for studying magnetotransport in high-mobility 2D materials, or magneto-optics in highly absorptive nominally nonmagnetic semiconductors. Using first-principles calculations, we show that the proximity exchange in monolayer MoSe$_2$ and WSe$_2$ due to ferromagnetic monolayer CrI$_3$ can be tuned (even qualitatively) by twisting and gating. Remarkably, the proximity exchange remains the same when using antiferromagnetic CrI$_3$ bilayer, paving the way for optical and electrical detection of layered antiferromagnets. Interestingly, the proximity exchange is *opposite* to the exchange of the adjacent antiferromagnetic layer. Finally, we show that the proximity exchange is confined to the layer adjacent to CrI$_3$, and that adding a separating hBN barrier drastically reduces the proximity effect. We complement our *ab initio* results with tight-binding modeling and solve the Bethe-Salpeter equation to provide experimentally verifiable optical signatures (in the exciton spectra) of the proximity exchange effects.

I. INTRODUCTION

Two-dimensional (2D) materials and their hybrids offer unforeseen opportunities, but also challenges, to electronics, spintronics, optics and magnetism [1–5]. Graphene, the prototypical 2D crystal, has excellent charge and spin transport properties [6–9], but lacks an orbital band gap needed for digital transistor applications. Fortunately, we have now available a large class of air-stable 2D semiconductors—transition-metal dichalcogenides (TMDCs)—which have a band gap in the optical range [10–14], and form a favorite platform for optical experiments including optical spin injection due to helicity-selective optical exitations [15]: electrons in opposite valleys, but at the same energy, feel opposite spin-orbit fields, pointing out of the plane. This effect is called valley Zeeman coupling; unlike true Zeeman field, the valley coupling preserves time reversal symmetry, since it stems from spin-orbit coupling (SOC).

In fact, one can create a *proximity structure* from graphene and a TMDC, initially proposed by DFT calculations [16] and confirmed experimentally [17,18] to facilitate transfer of the optically generated spin in TMDC into graphene. This is an example of a proximity effect [19] in van der Waals heterostructures. Proximity effects provide fascinating opportunities for *band-structure engineering*. Experiments and theory show that graphene can borrow different properties from a variety of substrates, be it SOC or magnetism [16,20–26].

For *all-2D spintronics*, it is desirable to integrate 2D materials such as graphene and TMDCs with 2D magnets. Experimentalists have demonstrated magnetic order in 2D layered crystals, such as MnSe$_2$ [27,28], CrGeTe$_3$ [29–34],

and CrI$_3$ [35–44], which are well suited for nanoelectronic devices [45]. Unlike thin films of conventional ferromagnets, which have magnetization typically in the plane (of the film), the 2D layered ferromagnets have magnetization pointing out of the plane, making them Ising-like.

This out-of-plane exchange interaction is a time-reversal breaking analog of the valley Zeeman splitting in TMDCs. The interplay of the two couplings, exchange and valley Zeeman, motivates explorations of stacked TMDCs and 2D ferromagnets. Certainly, one can introduce Zeeman coupling by applying an external magnetic field pointing out of the plane, but such fields produce modest valley splittings, about 0.1–0.2 meV per tesla [46–49]. Proximity exchange fields can induce much stronger effects, perhaps up to hundreds of meVs, without significantly altering the band structure of TMDCs [50–62]. Conventional ferromagnetic substrates, such as EuO or MnO, were predicted to give 200–300 meV [57–59]; experiments on EuS find only 2.5 meV [60], presumably due to uneven interfaces.

There already are experiments demonstrating proximity exchange in TMDCs. Recent measurements in TMDC/CrI$_3$ heterostructures [54,61] show a few meV of proximity exchange. CrI$_3$ is especially interesting, because the monolayer is a ferromagnet (FM) [39,63], while bilayer CrI$_3$ shows antiferromagnetic (AFM) coupling [39,64,65], in contradiction to the existing theory [41,63,66] which predicts a FM state for the low temperature phase. Remarkably, the magnetization of the CrI$_3$ can be tuned optically [61], thereby influencing proximity exchange and the photoluminescence (PL) spectrum of the TMDC. In addition, the magnetism in few layer CrI$_3$ can be controlled by gating and external magnetic fields [42,43], opening a new path for gate controlled devices, such as spin-filter tunnel junctions [65,67,68], and AFM spintronics [69,70].

*klaus.zollner@physik.uni-regensburg.de

Here, we provide a systematic theoretical analysis of the proximity exchange coupling in TMDC/CrI$_3$ heterostructures (with MoSe$_2$ and WSe$_2$ as TMDC) from first-principles. First, we confirm that the magnetic insulator substrate couples weakly to the TMDC by van der Waals forces, preserving the characteristic electronic band structure of the TMDC. The proximity exchange coupling splits the conduction (CB) and valence band (VB) of the TMDC by roughly 1–5 meV, and combined with the intrinsic (valley Zeeman) SOC of the TMDC lifts the valley degeneracy. We introduce a minimal model Hamiltonian to describe the proximity effects in TMDC due to CrI$_3$, extracting realistic proximity exchange parameters which should be useful for modeling transport and optics.

Next, and this is the main result of the paper, we find wide tunability of proximity exchange effects with respect of twisting and gating, and the absence of effects coming from additional layers (both TMDC and CrI$_3$). In particular, we find that *proximity exchange splittings depend on the twist angle* between the TMDC and the CrI$_3$. We investigated 0° and 30° structures, and observed that not only the magnitudes of the exchange differ, but, remarkably, the direction of the exchange field for holes changes sign. The exchange parameters can be tuned by a few meVs by gating, using accessible electric fields of a few V/nm.

It is rather fascinating that adding another layer of CrI$_3$ does not affect the proximity exchange in TMDCs (we used MoSe$_2$), given that the two magnetic layers are antiferromagnetically coupled and they have zero net magnetic moment. The proximity effect can then be used to detect, optically or electrically, the magnetic moment of the adjacent (to the TMDC) CrI$_3$ layer *even in the antiferromagnetic state*. We also explicitly prove the short-range nature of the proximity effects by investigating bilayer-MoSe$_2$/CrI$_3$ and MoSe$_2$/hBN/CrI$_3$. In the former, the proximity affects the adjacent TMDC layer, while in the latter the insulating hBN layer drastically reduces the proximity exchange. This message is important since experimentally it may be desirable to cover CrI$_3$ with hBN first, to improve its stability under ambient conditions. For proximity effects, using hBN barriers would be detrimental.

Finally, we give specific predictions for optical signatures of the proximity exchange effects, by calculating the excitonic absorption spectra employing the Bethe-Salpeter equation. The twist-angle and gate-bias dependence of the proximity exchange is mapped into the valley splitting of the first intralayer exciton peak. This is a valuable and experimentally testable fingerprint of our results.

II. BAND STRUCTURE, GEOMETRY, AND TWIST EFFECTS

To study proximity exchange effects, we set up a common unit cell for the TMDC/CrI$_3$ heterostructures (see Ref. [71]). We consider a 2×2 supercell for the TMDCs (MoSe$_2$ and WSe$_2$) above a 1×1 cell of CrI$_3$, as well as a larger 7×7 supercell of the TMDC on top of a $(2\sqrt{3} \times 2\sqrt{3})$R30° supercell of CrI$_3$. In Figs. 1(a) and 1(b), we show the geometry of the MoSe$_2$/CrI$_3$ heterostructure, as a typical structure of the small supercell with 0° twist angle. In Fig. 1(f), we show

the top view of the larger supercell which is twisted by 30° relative to the underlying CrI$_3$.

In Figs. 1(c)–1(e), we show the calculated band structure with a fit to our model Hamiltonian (see Ref. [71]) for the small MoSe$_2$/CrI$_3$ supercell structure without SOC (to extract the exchange coupling). We find that the bands of the TMDC are nicely preserved but are marked with a proximity exchange. The spin up CBs, originating from the CrI$_3$, are located within the band gap of the TMDC, see Fig. 1(c). In experiments it was already shown that the spin polarized in-gap states from the CrI$_3$ quench the PL spectrum for one light helicity only [54,61], due to additional nonradiative relaxation processes. The energy gap of the full heterostructure is $\Delta E \approx 400$ meV, as defined in Fig. 1(c). The band edges of the TMDC can be almost perfectly described by our model Hamiltonian, as shown in Figs. 1(d) and 1(e). Due to proximity exchange, the bands are spin split by about 5 meV.

In Figs. 1(g)–1(i), we present the calculated band structure with a fit to our model Hamiltonian for the larger MoSe$_2$/CrI$_3$ supercell structure with 30° twist angle without SOC. As there are much more atoms in the supercell, more in-gap states from the CrI$_3$ are located within the band gap of the TMDC. The proximity exchange is clearly visible. In comparison to the smaller, 0° supercell, the VB splitting is *opposite in sign*. Unfortunately, studying other, especially small twist angles is beyond our DFT approach. However, the different direction of the exchange field in VB seen for 0° and 30° structures shows that twisting can be an effective tool to modify the proximity effect. Similar effect was predicted in SOC proximity effect, by placing graphene on a topological insulator. Two different twist angles produced qualitatively different spin-orbit fields in graphene [72].

To investigate the optical signatures of the proximity exchange due to the twist angle, we calculate the absorption spectra of the intralayer excitons, i.e., electron-hole pairs created directly at the TMDC layer that are experimentally accessible in PL spectra [54,61]. For these calculations, we apply the effective Bethe-Salpeter equation [73–76] using the model Hamiltonian fitted to the first-principles band structure, see Figs. 1(d), 1(e), 1(h), and 1(i). For these calculations, we also consider the effects of SOC by combining the parameters summarized in Table I (see Ref. [71] for details of the excitonic calculations and the model Hamiltonian). Focusing on the lowest energy excitonic levels, we show in Figs. 1(j) and 1(k) the first absorption peak at K (σ_- polarization) and K' (σ_+ polarization) valleys for 0° and 30° twist angles. We find that the valley splitting (the energy separation between the two absorption peaks) shows a *substantial threefold increase* by changing the twist angle, from $\sim$1.13 meV for 0° to $\sim$3.89 meV for 30°. Interestingly, these energy splittings calculated within the single-particle picture ($\sim$1.25 meV for 0° and $\sim$4.29 meV for 30°) are in reasonable agreement with the excitonic calculations. We also performed a similar investigation for WSe$_2$/CrI$_3$ heterostructures and found an excitonic (single-particle) valley splitting of $\sim$1.43 (1.61) meV for 0° and $\sim$6.35 (7.09) meV for 30°, thus providing a dramatic $\sim$4.4-fold increase due to twist angle. In recent experiments by Zhong *et al.* [54], the measured valley splitting in WSe$_2$/CrI$_3$ is $\sim$3.5 meV (equivalent to $\sim$13 T external magnetic field in bare WSe$_2$), and thus it is reasonable to
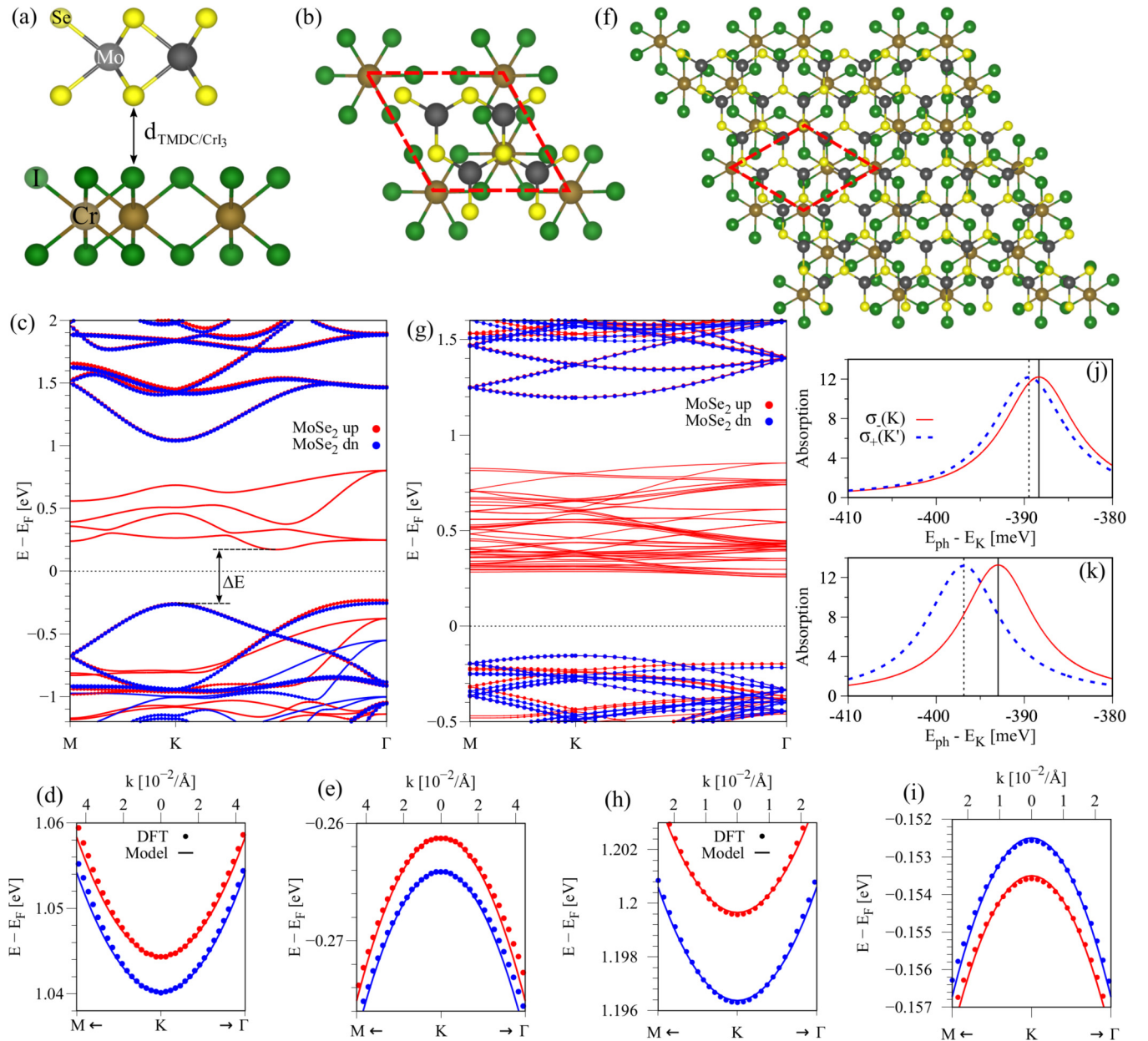
FIG. 1. Calculated band structures without SOC, geometries, and absorption spectra of $MoSe_2/CrI_3$. [(a) and (b)] Side and top view of the small supercell geometry (0° twist angle) with labels for the different atoms and the definition of the interlayer distance d_{TMDC/CrI_3}. One unit cell of CrI_3 is highlighted, by the red dashed line, in the top view. (c) Band structure along high-symmetry lines, with the energy gap of the heterostructure ΔE. The bands corresponding to $MoSe_2$ are emphasized by red (spin up) and blue (spin down) spheres. [(d) and (e)] Zoom to the CB and VB edge corresponding to $MoSe_2$. Symbols are DFT data and solid lines are the fitted model Hamiltonian. [(f)–(i)] The top view, calculated band structure, and the zoom to the low-energy bands for the larger supercell geometry (30° twist angle). [(j) and (k)] Calculated first absorption peak of intralayer excitons for small (b) and large (f) geometry (including SOC) with the vertical solid (dashed) arrows indicating the peak position for the absorption at K (K') point.

expect that the structure (or part of it, depending on the quality) was twisted. Undoubtedly, the WSe_2/CrI_3 heterostructure demands further experimental investigations of proximity exchange, especially with respect to different values of the twist angle. A similar twist angle dependence of proximity SOC has been reported for graphene/TMDC heterostructures [77].

As a magnetic field or proximity exchange breaks time-reversal symmetry, we show the calculated band structure for $MoSe_2/CrI_3$ with SOC in Fig. 2, for the 0° twist angle supercell. We find a very good agreement between the model Hamiltonian and the calculated bands around K and K' valley. The valley degeneracy is now broken, especially when comparing the CB edges at K and K' valley, see Figs. 2(b) and 2(c). Therefore a TMDC/CrI_3 heterostructure shows valley polarization of the TMDC, in agreement with recent measurements [54,61], and other first-principles calculations [78]. Inclusion

TABLE I. Summary of fit parameters, calculated dipoles and distances for TMDC/CrI$_3$ systems. The orbital gap Δ of the spectrum and the Fermi velocity v_F. The parameters λ_c and λ_v describe the SOC splittings, and B_c and B_v are the proximity exchange parameters for CB and VB. The dipole of the structures is given in debye and the distance $d_{\mathrm{TMDC/CrI_3}}$ is defined in Fig. 1(a). The twist angle 0° (30°) corresponds to the small (large) supercell in Fig. 1. The individual columns are for calculations of the bare TMDC (B) with the modified lattice constant from the heterostructure, the heterostructure without SOC (noSOC) and with SOC.

	MoSe$_2$/CrI$_3$			WSe$_2$/CrI$_3$			MoSe$_2$/CrI$_3$	WSe$_2$/CrI$_3$
dipole (Debye)		0.103			0.156		0.172	0.790
distance (Å)		3.506			3.497		3.517	3.529
twist angle (deg)		0			0		30	30
calculation	B	noSOC	SOC	B	noSOC	SOC	noSOC	noSOC
Δ (eV)	1.302	1.305	1.301	1.327	1.358	1.327	1.351	1.417
v_F (10^5 m/s)	4.591	4.579	4.591	5.863	5.799	5.845	4.597	5.863
λ_c (meV)	−9.647	–	−9.678	13.90	–	13.81	–	–
λ_v (meV)	94.56	–	94.43	241.79	–	240.99	–	–
λ_R (meV)	–	–	–	–	–	–	–	–
B_c (meV)	–	−2.081	−1.592	–	−2.223	−1.783	−1.641	−1.648
B_v (meV)	–	−1.454	−1.426	–	−1.446	−1.583	0.502	1.896

of SOC effects for the large supercell structure is beyond our computational possibilities and therefore not included here.

In order to qualitatively extract, the influence from the FM substrate, we calculate the band structure of the TMDC/CrI$_3$ heterostructures, for MoSe$_2$ and WSe$_2$ in the small supercell
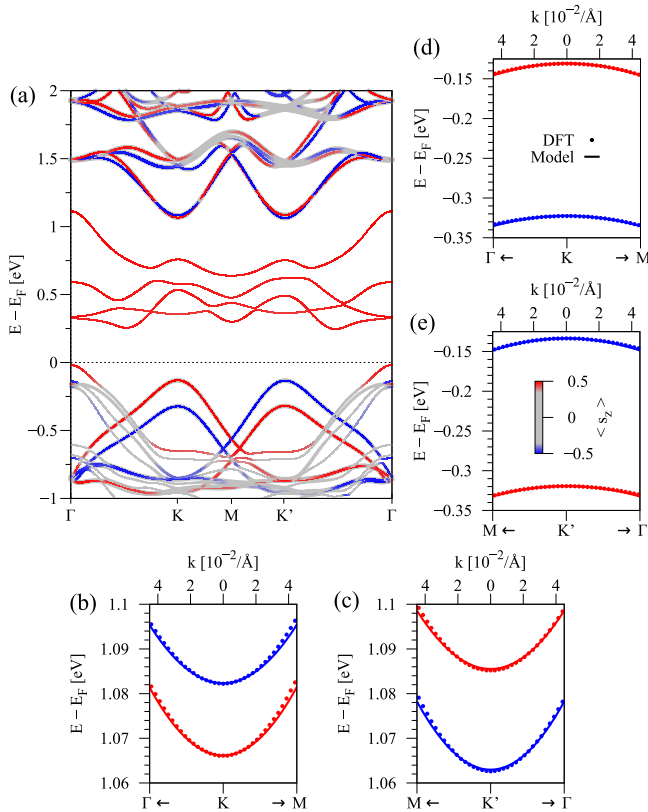

FIG. 2. Calculated band structure of MoSe$_2$/CrI$_3$ with SOC for the 0° twist angle structure. (a) Band structure along high-symmetry lines. Color corresponds to the s_z-expectation value. (b,c) Zoom to the CB edge corresponding to MoSe$_2$ at K and K'. Symbols are DFT data and solid lines are the fitted model Hamiltonian. [(d) and (e)] Same as (b) and (c) but for VB edge.

geometry, and fit it to our low-energy Hamiltonian [71]. To obtain reasonable fit parameters, we consider three situations. First, we calculate the band structure for the bare TMDC, removing the CrI$_3$, and check the SOC parameters for this situation, with the modified lattice constant used in the heterostructure geometry. This is crucial, because an increase in the lattice constant diminishes, for example, the band gap of the TMDC [79–82]. Second, we calculate the band structure for the TMDC/CrI$_3$ heterostructures without SOC in order to obtain the proximity exchange splitting parameters. Finally, we calculate the band structure for the TMDC/CrI$_3$ heterostructures with SOC. In Table I, we summarize the fit results for the three mentioned calculations, for 0° twist angle. Additionally, we give the fit results for the 30° twist angle case, corresponding to Figs. 1(f)–1(i) without SOC.

Especially interesting are the proximity exchange parameters, being roughly 2 meV in magnitude, translating into about 10 T exchange field [46–49], in agreement with recent experiments [54,61]. The calculation of the atomic magnetic moments reveals, that the magnetization direction of the TMDC is the same as in the I atoms, opposite to the Cr atoms, therefore giving *negative* proximity exchange parameters for a net CrI$_3$ magnetization pointing along positive z direction towards the TMDC. As there are many atoms in the unit cells, we calculate averaged magnetic moments for the different atomic species. The averaged magnetic moments for the small nontwisted supercell are Cr ($+3.53\,\mu_B$), I ($-0.19\,\mu_B$), Mo ($-0.0039\,\mu_B$), and Se ($-0.0046\,\mu_B$). We averaged only over Se atoms closer to the CrI$_3$ substrate, as they mediate the proximity exchange to the Mo atoms. The averaged magnetic moments for the large twisted supercell are Cr ($+3.46\,\mu_B$), I ($-0.18\,\mu_B$), Mo ($-0.0029\,\mu_B$), and Se ($-0.0031\,\mu_B$).

Including SOC in the heterostructure calculations, we find the parameters to be barely different than those from the individual calculations for the bare TMDCs or for the heterostructures without SOC. Therefore, combining the model Hamiltonian, the SOC parameters from the bare TMDC monolayer, and the exchange parameters from the heterostructure calculation without SOC, already suffices to get a reasonable low-energy band structure. Our fit shows that the
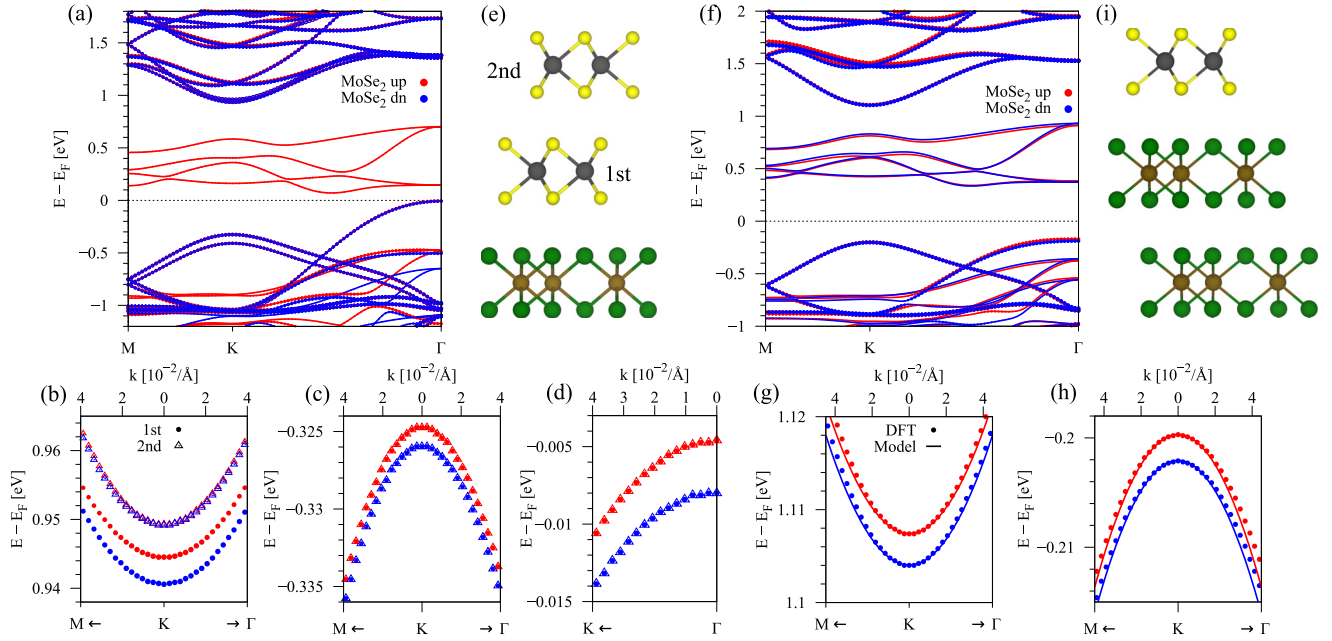
FIG. 3. (a) Band structure along high-symmetry lines for bilayer MoSe$_2$ on top of monolayer CrI$_3$. In (a)–(h), spin up (down) bands are plotted in red (blue), while symbols emphasize the character of the bands. In (a), the bands corresponding to bilayer MoSe$_2$ are emphasized by thicker spheres. (b) Zoom to the CB edge around the K point. [(c) and (d)] Same as (b), but for VB edge around K and Γ point. In (b)–(d), the bands corresponding to the first (second) layer of the bilayer MoSe$_2$ are emphasized by filled spheres (open triangles). (e) Side view of the geometry with definition of first and second layer of 2H bilayer MoSe$_2$. (f) Band structure along high-symmetry lines for monolayer MoSe$_2$ on top of bilayer CrI$_3$ in the AFM ($\uparrow\downarrow$) configuration. (g) Zoom to the CB edge around the K point (symbols), with a fit to the model Hamiltonian (solid line). (h) Same as (g), but for VB edge. (i) Side view of the geometry of monolayer MoSe$_2$ on bilayer CrI$_3$.

Rashba parameter is not necessary to capture the essentials of the band structure for the TMDC/CrI$_3$ stacks, because there is no in-plane component of the spin expectation value present around the band edges.

From the experimental point of view, when materials are mechanically exfoliated and stacked, one can expect various local interface (stacking) configurations between the TMDC and CrI$_3$, different to what is shown in Fig. 1(b). However, our calculations show that proximity exchange splittings are marginally affected by different interface configurations, see Ref. [71].

III. SHORT-RANGENESS OF PROXIMITY EFFECTS

A. Bilayer TMDC on monolayer CrI$_3$

In experiment, when the TMDC is exfoliated from bulk crystals, it may also happen that a bilayer TMDC is transferred onto the magnetic CrI$_3$ substrate. Does the second TMDC layer also experience proximity exchange, or only the closest layer? To answer this question, we consider 2H bilayer MoSe$_2$ on top of monolayer CrI$_3$. We first allow for relaxation of the whole geometry, similar to the monolayer MoSe$_2$ case, to get reasonable interlayer distances.

In Fig. 3(a), we show the calculated band structure of 2H bilayer MoSe$_2$ on top of monolayer CrI$_3$ without considering SOC effects. The bilayer TMDC has an indirect band gap, consistent with literature [83,84]. For the CB edge, see Fig. 3(b), we can identify the bands originating from the first and second layer of the bilayer MoSe$_2$. The bands from the first layer are spin-split, similar to what we observe for the

monolayer MoSe$_2$ case, while the bands originating from the second layer experience negligible splitting. The VB edge around the K point, see Fig. 3(c), is formed by two nondegenerate bands, a spin up and a spin down one, which are split in energy. The magnitude of the splitting is again similar to the monolayer case and a result of proximity exchange. However, we find that each band is formed by orbitals from both TMDC layers, which does not allow us to trace back the splitting to proximity exchange in a specific layer. For further insights, we show the calculated layer- and spin-resolved density of states, see Ref. [71]. In additon, the calculated magnetic moments for the second layer ($-0.0001\,\mu_B$) are much smaller than for the first layer ($-0.004\,\mu_B$). Thus we conclude that the proximity exchange is mainly induced in the TMDC layer closest to the CrI$_3$ substrate.

B. TMDC on antiferromagnetic bilayer CrI$_3$

Another feature which was especially observed in bilayer CrI$_3$ is the switching from FM to AFM coupled layers by gating [39,42]. For the AFM state, there are two energetically degenerate states of the bilayer (first layer $\uparrow$, second layer $\downarrow$, or vice versa). Therefore we calculate the band structure, with and without SOC, for MoSe$_2$ on top of bilayer CrI$_3$, which is stacked in the low temperature rhombohedral phase [41,63,66]. We find a total energy difference of $E_{\mathrm{AFM}} - E_{\mathrm{FM}} \approx 24$ meV between the FM and the AFM state calculated without SOC of the whole TMDC/bilayer-CrI$_3$ stack, which contains four Cr atoms in our supercell. In agreement with previous DFT calculations [41,63,66], we find that the FM

state of the bilayer CrI_3 is energetically favorable compared to the AFM state in contrast to experiments [39,64,65].

In Fig. 3(f), we show the calculated band structure of $MoSe_2$ on top of bilayer CrI_3 without SOC, when the bilayer CrI_3 is in the AFM ($\uparrow\downarrow$) configuration (the magnetization of the CrI_3 layer directly below the TMDC is pointing $\uparrow$). In Ref. [71], we show the band structures including SOC for both cases, the FM and AFM configuration. The fit to the low-energy bands, see Figs. 3(g) and 3(h) are similar to what is shown in Fig. 1 for $MoSe_2$ on top of monolayer CrI_3. The naive expectation is that, depending on the total magnetization of the bilayer CrI_3, we can enhance or reduce proximity exchange in the TMDC, compared to the monolayer CrI_3 case. However, we find that the FM ($\uparrow\uparrow$) or AFM ($\uparrow\downarrow$) coupled bilayer give almost no difference in the fit parameters compared to the monolayer case [71].

C. Effects of hBN barrier

Finally, when introducing a hBN buffer layer between the $MoSe_2$ and CrI_3, proximity exchange splittings of the $MoSe_2$ bands are drastically reduced to about 100 μeV [71]. The calculated averaged magnetic moments for the case of $MoSe_2$/hBN/CrI_3 are Cr ($+3.50\,\mu_B$), I ($-0.19\,\mu_B$), N ($-0.0016\,\mu_B$), B ($0.0\,\mu_B$), Mo ($-0.0001\,\mu_B$), and Se ($-0.0001\,\mu_B$). The magnetic moments in the TMDC are reduced by one order of magnitude, compared to the case without the hBN layer. By looking at the proximity exchange in the hBN layer, we find that the bands originating from hBN are strongly hybridized with the CrI_3 bands, see Ref. [71]. This can be helpful for interpreting tunneling experiments of such heterostructures. All these results indicate that proximity exchange is truly a short range effect, and can be used to create and detect the magnetic order in the layered AFM, bilayer CrI_3 [71].

IV. GATE TUNABLE PROXIMITY EXCHANGE AND EXCITON SPLITTING

Motivated by recent experiments [39,42,43], showing the electric field control of magnetism in few layer CrI_3, and the optical tuning of proximity exchange in TMDC/CrI_3 heterostructures [61], we perform additional calculations for our heterostructures, where we apply a transverse electric field across the geometry consisting of one monolayer of TMDC and one of CrI_3.

As calculations without SOC already give reasonable proximity exchange parameters, we neglect SOC for the electric field study. In Fig. 4, we show the fit parameters as a function of a transverse electric field for TMDC/CrI_3 heterostructures calculated without SOC, for the $0°$ twist angle structures. We find that the gap parameter Δ, as well as the Fermi velocity v_F are barely affected by external electric fields. The dipole of the heterostructure depends linearly on the electric field. By applying an electric field, the band offsets can be changed. The band gap ΔE of the heterostructure, defined in Fig. 1(c), shrinks linearly with applied electric field. This tunability of the band offsets could be very important for other effects. Imagine electrons located in the CrI_3 layer coupled to holes in the TMDC layer. As we apply an electric field, we tune
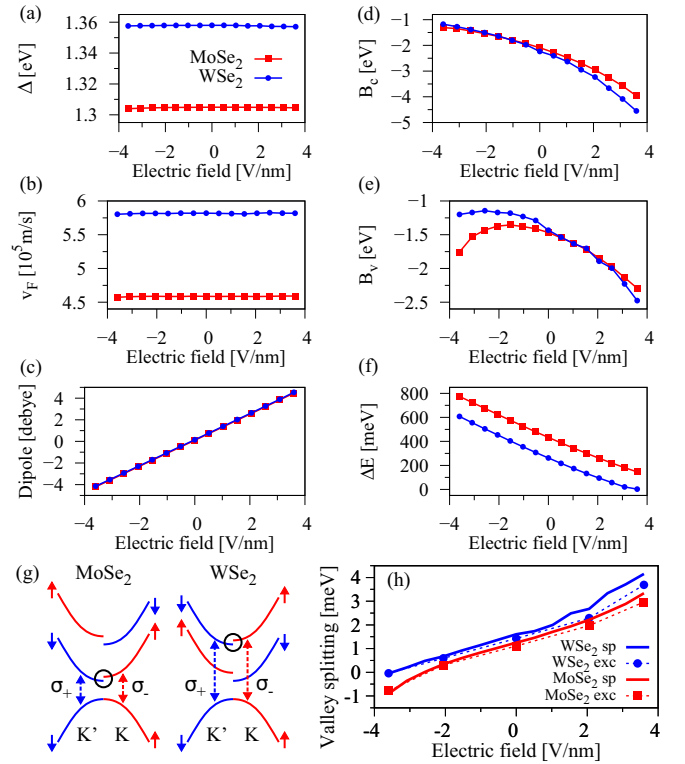

FIG. 4. Fit parameters as a function of transverse electric field for TMDC/CrI_3 heterostructures for calculations without SOC. (a) The orbital gap Δ of the spectrum, (b) the Fermi velocity v_F, (c) the dipole of the heterostructure, [(d) and (e)] the proximity exchange parameters B_c and B_v, and (f) the band gap ΔE, as defined in Fig. 1(c). (g) Schematic representation of the exchange interaction in the band structure of $MoSe_2$ and WSe_2 at K and K' points depicting the lowest energy optically allowed transitions (vertical dashed arrows). (h) Single-particle and intralayer exciton valley splitting for the first active optical transition between the top VB and the first (second) CB in $MoSe_2$ (WSe_2) [indicated by the circle in (g)] as function of the external electric field. For the excitons, the valley splitting is taken as the energy difference between the first absorption peaks (see Fig. 1 and Ref. [71]).

the band gap ΔE, possibly affecting the lifetime of interlayer excitons. Especially interesting is the fact that the CB states, originating from the CrI_3, are spin polarized, see Fig. 1(c), which then gives additional valley control, depending on the magnetization of the CrI_3, due to spin-valley coupling in the TMDC. Most important, the two exchange parameters B_c and B_v can be tuned by the external electric field. In general, the proximity exchange increases, when the electric field is tuned from negative to positive values, which enables the gate control of proximity exchange.

Let us now look at the tunability of proximity exchange reflected in the valley splitting of the TMDC intralayer excitons. In Fig. 4(g), we sketch the energy levels for the top VB and first two CBs at K and K' valleys for $MoSe_2$ and WSe_2. We set the top VB to zero, which simplifies the analysis by just looking at the allowed optical transitions that satisfy the spin-valley locking. The effective signature of proximity is the interplay of SOC and exchange parameters in the optically allowed transitions from the VB to the first (second) CB in

MoSe$_2$ (WSe$_2$). The resulting valley splittings are shown in Fig. 4(h) for the first exciton absorption peak (dashed lines with points) and the single particle of the optically active bands (solid lines). Unlike the strong nonlinear behavior observed in the exchange parameters B_c and B_v under applied electric field, see Figs. 4(d)–4(e), the optical valley splitting due the proximity exchange shows a rather linear behavior, with the single-particle results following closely the excitonic calculations. Specifically for MoSe$_2$, the valley splitting changes sign at an electric field of about -2.5 V/nm. This trend might also happen for WSe$_2$ for further negative values of electric field. Therefore, in addition to the control of the twist angle, see Figs. 1(j) and 1(k), the application of external electric fields can modify the value of the valley splitting. In real samples, it is reasonable to expect an interplay of both effects, the twist angle and the electric field. Regarding the parameters used in the calculations shown in Fig. 4(h), we used the model Hamiltonian with the values of Δ, v_F, λ_c, λ_v given in Table I with SOC and B_c, B_v extracted from the data presented in Figs. 4(d) and 4(e). See Ref. [71] for details and the calculated absorption spectra used to extract the exciton valley splittings.

Finally, we want to discuss several experimental uncertainties, one has to consider, before directly comparing them with our results. For example, the twist angle and a resulting moirè pattern between the TMDC and CrI$_3$ in micrometer size samples, can influence proximity exchange. We have seen that the twist angle can lead to a giant enhancement of the valley splitting. However, when twist angle is not an issue and can be precisely controlled in experiment, there are still several different local interface configurations. We have studied this as different interface geometries of the small supercell in Ref. [71]. Local variations in the magnitude of the proximity exchange and valley splitting can occur. One can even speculate about a vanishing global proximity exchange in the TMDC, when thinking of magnetic domains in the CrI$_3$ substrate. We have also seen, that proximiy exchange depends on the actual electric dipole field across the sample. In contrast to our approach of mono- and bilayer CrI$_3$ as substrate, experiments may utilize thicker CrI$_3$ samples (few layers) affecting the overall electrostatics and the band alignment in the heterostructure. In this context, one must also consider the effect of an additional SiO$_2$ or hBN substrate/capping layer to protect the system from the environment. In additon, recent first-principles calculations have shown that the optical and magneto-optical properties of CrI$_3$ are also dominated by strongly bound excitons [44]. When studying the absorption spectra of TMDC/CrI$_3$ heterostructures, one has to be aware that quasiparticles can in principle be created in both layers simultaneously. We conclude that experimentally (and also theoretically) one has to be very careful in preparing the heterostructures and analyzing the data, in order to make qualitative statements about the proximity exchange effects. Even though our presented analysis is very systematic, we can at most give predictions for idealized structures.

V. SUMMARY

By combining DFT calculations with a low-energy model Hamiltonian of exchange proximitized TMDCs, we have shown that a CrI$_3$ substrate causes sizable proximity exchange in the TMDCs MoSe$_2$ and WSe$_2$. Crucial for the magnitude of the induced valley splitting, is the twist angle between the TMDC and CrI$_3$, as we find from the $0°$ and $30°$ twist angle cases, by calculating optical absorption spectra. By applying experimentally accessible electric fields transverse to the heterostructure, we can tune band offsets, proximity exchange, and consequently the valley splitting in the TMDCs. Finally, we have seen that proximity exchange originates only from the FM CrI$_3$-layer closest to the TMDC by investigating TMDC/bilayer-CrI$_3$ heterostructures. The observed twist angle dependence, electric field tunability, and short-rangeness of proximity exchange are experimentally testable fingerprints of our results, and should be generally valid for other 2D van der Waals heterostructures.

[1] G. Fiori, F. Bonaccorso, G. Iannaccone, T. Palacios, D. Neumaier, A. Seabaugh, S. K. Banerjee, and L. Colombo, Nat. Nanotechnol. **9**, 768 (2014).

[2] A. C. Ferrari, F. Bonaccorso, V. Fal'ko, K. S. Novoselov, S. Roche, P. Bøggild, S. Borini, F. H. L. Koppens, V. Palermo, N. Pugno, J. A. Garrido, R. Sordan, A. Bianco, L. Ballerini, M. Prato, E. Lidorikis, J. Kivioja, C. Marinelli, T. Ryhänen, A. Morpurgo, J. N. Coleman, V. Nicolosi, L. Colombo, A. Fert, M. Garcia-Hernandez, A. Bachtold, G. F. Schneider, F. Guinea, C. Dekker, M. Barbone, Z. Sun, C. Galiotis, A. N. Grigorenko, G. Konstantatos, A. Kis, M. Katsnelson, L. Vandersypen, A. Loiseau, V. Morandi, D. Neumaier, E. Treossi, V. Pellegrini, M. Polini, A. Tredicucci, G. M. Williams, B. Hee Hong, J.-H. Ahn, J. Min Kim, H. Zirath, B. J. van Wees, H. van der Zant, L. Occhipinti,

A. Di Matteo, I. A. Kinloch, T. Seyller, E. Quesnel, X. Feng, K. Teo, N. Rupesinghe, P. Hakonen, S. R. T. Neil, Q. Tannock, T. Löfwander, and J. Kinaret, Nanoscale **7**, 4598 (2015).

[3] W. Choi, N. Choudhary, G. H. Han, J. Park, D. Akinwande, and Y. H. Lee, Mater. Today **20**, 116 (2017).

[4] F. Schwierz, J. Pezoldt, and R. Granzner, Nanoscale **7**, 8261 (2015).

[5] I. Žutić, J. Fabian, and S. Das Sarma, Rev. Mod. Phys. **76**, 323 (2004).

[6] M. Gurram, S. Omar, and B. J. van Wees, 2D Mater. **5**, 032004 (2018).

[7] A. H. Castro Neto, F. Guinea, N. M. R. Peres, K. S. Novoselov, and A. K. Geim, Rev. Mod. Phys. **81**, 109 (2009).

[8] S. Das Sarma, S. Adam, E. H. Hwang, and E. Rossi, Rev. Mod. Phys. **83**, 407 (2011).

[9] W. Han, R. K. Kawakami, M. Gmitra, and J. Fabian, Nat. Nano. **9**, 794 (2014).

[10] A. Kormányos, G. Burkard, M. Gmitra, J. Fabian, V. Zólyomi, N. D. Drummond, V. Fal'ko, and V. Fal'ko, 2D Mater. **2**, 022001 (2014).

[11] G.-B. Liu, D. Xiao, Y. Yao, X. Xu, and W. Yao, Chem. Soc. Rev. **44**, 2643 (2015).

[12] P. Tonndorf, R. Schmidt, P. Böttger, X. Zhang, J. Börner, A. Liebig, M. Albrecht, C. Kloc, O. Gordan, D. R. T. Zahn, S. Michaelis de Vasconcellos, and R. Bratschitsch, Opt. Express **21**, 4908 (2013).

[13] S. Tongay, J. Zhou, C. Ataca, K. Lo, T. S. Matthews, J. Li, J. C. Grossman, and J. Wu, Nano Lett. **12**, 5576 (2012).

[14] G. Eda, H. Yamaguchi, D. Voiry, T. Fujita, M. Chen, and M. Chhowalla, Nano Lett. **11**, 5111 (2011).

[15] D. Xiao, G.-B. Liu, W. Feng, X. Xu, and W. Yao, Phys. Rev. Lett. **108**, 196802 (2012).

[16] M. Gmitra and J. Fabian, Phys. Rev. B **92**, 155403 (2015).

[17] Y. K. Luo, J. Xu, T. Zhu, G. Wu, E. J. McCormick, W. Zhan, M. R. Neupane, and R. K. Kawakami, Nano Lett. **17**, 3877 (2017).

[18] A. Avsar, D. Unuchek, J. Liu, O. L. Sanchez, K. Watanabe, T. Taniguchi, B. Özyilmaz, and A. Kis, ACS Nano **11**, 11678 (2017).

[19] I. Žutić, A. Matos-Abiague, B. Scharf, H. Dery, and K. Belashchenko, Mater. Today **22**, 85 (2018).

[20] K. Zollner, M. Gmitra, T. Frank, and J. Fabian, Phys. Rev. B **94**, 155441 (2016).

[21] Z. Qiao, W. Ren, H. Chen, L. Bellaiche, Z. Zhang, A. H. MacDonald, and Q. Niu, Phys. Rev. Lett. **112**, 116404 (2014).

[22] J. Zhang, B. Zhao, T. Zhou, Y. Xue, C. Ma, and Z. Yang, Phys. Rev. B **97**, 085401 (2018).

[23] D. V. Averyanov, I. S. Sokolov, A. M. Tokmachev, O. E. Parfenov, I. A. Karateev, A. N. Taldenkov, and V. G. Storchak, ACS Appl. Mater. Interfaces **10**, 20767 (2018).

[24] D. Khokhriakov, A. W. Cummings, K. Song, M. Vila, B. Karpiak, A. Dankert, S. Roche, and S. P. Dash, Sci. Adv. **4**, eaat9349 (2018).

[25] A. Hallal, F. Ibrahim, H. Yang, S. Roche, and M. Chshiev, 2D Mater. **4**, 025074 (2017).

[26] C. Cardoso, D. Soriano, N. A. García-Martínez, and J. Fernández-Rossier, Phys. Rev. Lett. **121**, 067701 (2018).

[27] D. J. O'Hara, T. Zhu, A. H. Trout, A. S. Ahmed, Y. K. Luo, C. H. Lee, M. R. Brenner, S. Rajan, J. A. Gupta, D. W. McComb, and R. K. Kawakami, Nano Lett. **18**, 3125 (2018).

[28] M. Kan, S. Adhikari, and Q. Sun, Phys. Chem. Chem. Phys. **16**, 4990 (2014).

[29] X. Li and J. Yang, J. Mater. Chem. C **2**, 7071 (2014).

[30] V. Carteaux, D. Brunet, G. Ouvrard, and G. Andre, J. Phys.: Condens. Matter **7**, 69 (1995).

[31] C. Gong, L. Li, Z. Li, H. Ji, A. Stern, Y. Xia, T. Cao, W. Bao, C. Wang, Y. Wang, Z. Q. Qiu, R. J. Cava, S. G. Louie, J. Xia, and X. Zhang, Nature (London) **546**, 265 (2017).

[32] B. Siberchicot, S. Jobic, V. Carteaux, P. Gressier, and G. Ouvrard, J. Phys. Chem. **100**, 5863 (1996).

[33] G. T. Lin, H. L. Zhuang, X. Luo, B. J. Liu, F. C. Chen, J. Yan, Y. Sun, J. Zhou, W. J. Lu, P. Tong, Z. G. Sheng, Z. Qu, W. H. Song, X. B. Zhu, and Y. P. Sun, Phys. Rev. B **95**, 245212 (2017).

[34] Z. Wang, T. Zhang, M. Ding, B. Dong, Y. Li, M. Chen, X. Li, J. Huang, H. Wang, X. Zhao, Y. Li, D. Li, C. Jia, L. Sun, H. Guo, Y. Ye, D. Sun, Y. Chen, T. Yang, J. Zhang, S. Ono, Z. Han, and Z. Zhang, Nat. Nanotech. **13**, 554 (2018).

[35] J. Liu, Q. Sun, Y. Kawazoe, and P. Jena, Phys. Chem. Chem. Phys. **18**, 8777 (2016).

[36] W.-B. Zhang, Q. Qu, P. Zhu, and C.-H. Lam, J. Mater. Chem. C **3**, 12457 (2015).

[37] M. A. McGuire, H. Dixit, V. R. Cooper, and B. C. Sales, Chem. Mater. **27**, 612 (2015).

[38] L. Webster, L. Liang, and J. A. Yan, Phys. Chem. Chem. Phys. **20**, 23546 (2018).

[39] B. Huang, G. Clark, E. Navarro-Moratalla, D. R. Klein, R. Cheng, K. L. Seyler, D. Zhong, E. Schmidgall, M. A. McGuire, D. H. Cobden, W. Yao, D. Xiao, P. Jarillo-Herrero, and X. Xu, Nature (London) **546**, 270 (2017).

[40] P. Jiang, L. Li, Z. Liao, Y. Zhao, and Z. Zhong, Nano Lett. **18**, 3844 (2018).

[41] D. Soriano, C. Cardoso, and J. Fernández-Rossier, Solid State Commun. **299**, 113662 (2019).

[42] B. Huang, G. Clark, D. R. Klein, D. MacNeill, E. Navarro-Moratalla, K. L. Seyler, N. Wilson, M. A. McGuire, D. H. Cobden, D. Xiao, W. Yao, P. Jarillo-Herrero, and X. Xu, Nat. Nanotech. **13**, 544 (2018).

[43] S. Jiang, L. Li, Z. Wang, K. F. Mak, and J. Shan, Nat. Nanotech. **13**, 549 (2018).

[44] M. Wu, Z. Li, T. Cao, and S. G. Louie, Nat. Commun. **10**, 1 (2019).

[45] K. S. Burch, D. Mandrus, and J.-G. Park, Nature (London) **563**, 47 (2018).

[46] A. Srivastava, M. Sidler, A. V. Allain, D. S. Lembke, A. Kis, and A. Imamoğlu, Nat. Phys. **11**, 141 (2015).

[47] G. Aivazian, Z. Gong, A. M. Jones, R. L. Chu, J. Yan, D. G. Mandrus, C. Zhang, D. Cobden, W. Yao, and X. Xu, Nat. Phys. **11**, 148 (2015).

[48] Y. Li, J. Ludwig, T. Low, A. Chernikov, X. Cui, G. Arefe, Y. D. Kim, A. M. van der Zande, A. Rigosi, H. M. Hill, S. H. Kim, J. Hone, Z. Li, D. Smirnov, and T. F. Heinz, Phys. Rev. Lett. **113**, 266804 (2014).

[49] D. MacNeill, C. Heikes, K. F. Mak, Z. Anderson, A. Kormányos, V. Zólyomi, J. Park, and D. C. Ralph, Phys. Rev. Lett. **114**, 037401 (2015).

[50] S. A. Vitale, D. Nezich, J. O. Varghese, P. Kim, N. Gedik, P. Jarillo-Herrero, D. Xiao, and M. Rothschild, Small **14**, 1801483 (2018).

[51] F. Langer, C. P. Schmid, S. Schlauderer, M. Gmitra, J. Fabian, P. Nagler, C. Schüller, T. Korn, P. G. Hawkins, J. T. Steiner, U. Huttner, S. W. Koch, M. Kira, and R. Huber, Nature (London) **557**, 76 (2018).

[52] J. R. Schaibley, H. Yu, G. Clark, P. Rivera, J. S. Ross, K. L. Seyler, W. Yao, and X. Xu, Nat. Rev. Mater. **1**, 16055 (2016).

[53] Y. Ye, J. Xiao, H. Wang, Z. Ye, H. Zhu, M. Zhao, Y. Wang, J. Zhao, X. Yin, and X. Zhang, Nat. Nanotech. **11**, 598 (2016).

[54] D. Zhong, K. L. Seyler, X. Linpeng, R. Cheng, N. Sivadas, B. Huang, E. Schmidgall, T. Taniguchi, K. Watanabe, M. A. McGuire, W. Yao, D. Xiao, K.-M. C. Fu, and X. Xu, Sci. Adv. **3**, e1603113 (2017).

[55] Y. Ji, Y. Song, J. Zou, and W. Mi, Phys. Chem. Chem. Phys. **20**, 6100 (2018).

[56] N. Li, J. Zhang, Y. Xue, T. Zhou, and Z. Yang, Phys. Chem. Chem. Phys. **20**, 3805 (2018).

[57] J. Qi, X. Li, Q. Niu, and J. Feng, Phys. Rev. B **92**, 121403(R) (2015).

[58] Q. Zhang, S. A. Yang, W. Mi, Y. Cheng, and U. Schwingenschlögl, Adv. Mater. **28**, 959 (2016).

[59] L. Xu, M. Yang, L. Shen, J. Zhou, T. Zhu, and Y. P. Feng, Phys. Rev. B **97**, 041405(R) (2018).

[60] C. Zhao, T. Norden, P. Zhang, P. Zhao, Y. Cheng, F. Sun, J. P. Parry, P. Taheri, J. Wang, Y. Yang, T. Scrace, K. Kang, S. Yang, G. X. Miao, R. Sabirianov, G. Kioseoglou, W. Huang, A. Petrou, and H. Zeng, Nat. Nanotech. **12**, 757 (2017).

[61] K. L. Seyler, D. Zhong, B. Huang, X. Linpeng, N. P. Wilson, T. Taniguchi, K. Watanabe, W. Yao, D. Xiao, M. A. McGuire, K.-M. C. Fu, and X. Xu, Nano Lett. **18**, 3823 (2018).

[62] B. Peng, Q. Li, X. Liang, P. Song, J. Li, K. He, D. Fu, Y. Li, C. Shen, H. Wang, C. Wang, T. Liu, L. Zhang, H. Lu, X. Wang, J. Zhao, J. Xie, M. Wu, L. Bi, L. Deng, and K. P. Loh, ACS Nano **11**, 12257 (2017).

[63] P. Jiang, C. Wang, D. Chen, Z. Zhong, Z. Yuan, Z.-Y. Lu, and W. Ji, Phys. Rev. B **99**, 144401 (2019).

[64] S. Jiang, J. Shan, and K. F. Mak, Nat. Mater. **17**, 406 (2018).

[65] T. Song, X. Cai, M. W.-Y. Tu, X. Zhang, B. Huang, N. P. Wilson, K. L. Seyler, L. Zhu, T. Taniguchi, K. Watanabe, M. A. McGuire, D. H. Cobden, D. Xiao, W. Yao, and X. Xu, Science **360**, 1214 (2018).

[66] N. Sivadas, S. Okamoto, X. Xu, C. J. Fennie, and D. Xiao, Nano Lett. **18**, 7658 (2018).

[67] D. R. Klein, D. MacNeill, J. L. Lado, D. Soriano, E. Navarro-Moratalla, K. Watanabe, T. Taniguchi, S. Manni, P. Canfield, J. Fernández-Rossier, and P. Jarillo-Herrero, Science **360**, 1218 (2018).

[68] D. Ghazaryan, M. T. Greenaway, Z. Wang, V. H. Guarochico-Moreira, I. J. Vera-Marun, J. Yin, Y. Liao, S. V. Morozov, O. Kristanovski, A. I. Lichtenstein, M. I. Katsnelson, F. Withers, A. Mishchenko, L. Eaves, A. K. Geim, K. S. Novoselov, and A. Misra, Nat. Electron. **1**, 344 (2018).

[69] V. Baltz, A. Manchon, M. Tsoi, T. Moriyama, T. Ono, and Y. Tserkovnyak, Rev. Mod. Phys. **90**, 015005 (2018).

[70] T. Jungwirth, X. Marti, P. Wadley, and J. Wunderlich, Nat. Nanotech. **11**, 231 (2016).

[71] See Supplemental Material at http://link.aps.org/supplemental/10.1103/PhysRevB.100.085128, including Refs. [10,35–40,42,43,54,57,61,64,72–76,85–112], for details about the used supercell geometries, the computational methods, model Hamiltonian, and further calculation results.

[72] K. Song, D. Soriano, A. W. Cummings, R. Robles, P. Ordejón, and S. Roche, Nano Lett. **18**, 2033 (2018).

[73] M. Rohlfing and S. G. Louie, Phys. Rev. B **62**, 4927 (2000).

[74] B. Scharf, G. Xu, A. Matos-Abiague, and I. Žutić, Phys. Rev. Lett. **119**, 127403 (2017).

[75] D. Tedeschi, M. De Luca, P. E. Faria Junior, A. Granados del Águila, Q. Gao, H. H. Tan, B. Scharf, P. C. M. Christianen, C. Jagadish, J. Fabian, and A. Polimeni, Phys. Rev. B **99**, 161204(R) (2019).

[76] P. E. Faria Junior, M. Kurpas, M. Gmitra, and J. Fabian, arXiv:1904.10328.

[77] Y. Li and M. Koshino, Phys. Rev. B **99**, 075438 (2019).

[78] C. Lin, Y. Li, Q. Wei, Q. Shen, Y. Cheng, and W. Huang, ACS Appl. Mater. Interfaces **11**, 18858 (2019).

[79] S. Fang, S. Carr, M. A. Cazalilla, and E. Kaxiras, Phys. Rev. B **98**, 075106 (2018).

[80] D. Lloyd, X. Liu, J. W. Christopher, L. Cantley, A. Wadehra, B. L. Kim, B. B. Goldberg, A. K. Swan, and J. S. Bunch, Nano Lett. **16**, 5836 (2016).

[81] R. Frisenda, M. Drüppel, R. Schmidt, S. Michaelis de Vasconcellos, D. Perez de Lara, R. Bratschitsch, M. Rohlfing, and A. Castellanos-Gomez, npj 2D Mater. Appl. **1**, 10 (2017).

[82] G. Plechinger, A. Castellanos-Gomez, M. Buscema, H. S. J. van der Zant, G. A. Steele, A. Kuc, T. Heine, C. Schüller, and T. Korn, 2D Mater. **2**, 015006 (2015).

[83] A. Kormányos, V. Zólyomi, V. I. Fal'ko, and G. Burkard, Phys. Rev. B **98**, 035408 (2018).

[84] F. Bussolotti, H. Kawai, Z. E. Ooi, V. Chellappan, D. Thian, A. L. C. Pang, and K. E. J. Goh, Nano Futur. **2**, 032001 (2018).

[85] S. R. Bahn and K. W. Jacobsen, Comput. Sci. Eng. **4**, 56 (2002).

[86] W. J. Schutte, J. L. De Boer, and F. Jellinek, J. Solid State Chem. **70**, 207 (1987).

[87] P. B. James and M. T. Lavik, Acta Crystallogr. **16**, 1183 (1963).

[88] P. Hohenberg and W. Kohn, Phys. Rev. **136**, B864 (1964).

[89] P. Giannozzi, S. Baroni, N. Bonini, M. Calandra, R. Car, C. Cavazzoni, D. Ceresoli, G. L. Chiarotti, M. Cococcioni, I. Dabo, A. D. Corso, S. Fabris, G. Fratesi, S. de Gironcoli, R. Gebauer, U. Gerstmann, C. Gougoussis, A. Kokalj, M. Lazzeri, L. Martin-Samos, N. Marzari, F. Mauri, R. Mazzarello, S. Paolini, A. Pasquarello, L. Paulatto, C. Sbraccia, S. Scandolo, G. Sclauzero, A. P. Seitsonen, A. Smogunov, P. Umari, and R. M. Wentzcovitch, J. Phys.: Condens. Matter **21**, 395502 (2009).

[90] G. Kresse and D. Joubert, Phys. Rev. B **59**, 1758 (1999).

[91] J. P. Perdew, K. Burke, and M. Ernzerhof, Phys. Rev. Lett. **77**, 3865 (1996).

[92] A. I. Liechtenstein, V. I. Anisimov, and J. Zaanen, Phys. Rev. B **52**, R5467 (1995).

[93] S. Grimme, J. Comput. Chem. **27**, 1787 (2006).

[94] V. Barone, M. Casarin, D. Forrer, M. Pavone, M. Sambi, and A. Vittadini, J. Comput. Chem. **30**, 934 (2009).

[95] L. Bengtsson, Phys. Rev. B **59**, 12301 (1999).

[96] N. S. Rytova, Moscow Univ. Phys. Bull. **3**, 18 (1967).

[97] L. V. Keldysh, Pis'ma Zh. Eksp. Teor. Fiz. **29**, 716 (1979) [Sov. J. Exp. Theor. Phys. Lett. **29**, 658 (1979)].

[98] P. Cudazzo, I. V. Tokatly, and A. Rubio, Phys. Rev. B **84**, 085406 (2011).

[99] T. C. Berkelbach, M. S. Hybertsen, and D. R. Reichman, Phys. Rev. B **88**, 045318 (2013).

[100] H. Haug and S. W. Koch, *Quantum Theory of the Optical and Electronic Properties of Semiconductors*, 5th ed. (World Scientific, Singapore, 2009).

[101] B. Scharf, D. Van Tuan, I. Žutić, and H. Dery, J. Phys.: Condens. Matter **31**, 203001 (2019).

[102] Z. Zhang, X. Ni, H. Huang, L. Hu, and F. Liu, Phys. Rev. B **99**, 115441 (2019).

[103] A. Catellani, M. Posternak, A. Baldereschi, and A. J. Freeman, Phys. Rev. B **36**, 6105 (1987).

[104] F. Dirnberger, M. Kammermeier, J. König, M. Forsch, P. E. Faria Junior, T. Campos, J. Fabian, J. Schliemann, C. Schüller,

T. Korn, P. Wenk, and D. Bougeard, Appl. Phys. Lett. **114**, 202101 (2019).

[105] M. McGuire, Crystals **7**, 121 (2017).

[106] L. Webster and J.-A. Yan, Phys. Rev. B **98**, 144411 (2018).

[107] L. L. Handy and N. W. Gregory, J. Am. Chem. Soc. **74**, 891 (1952).

[108] N. Wakabayashi, H. G. Smith, and R. M. Nicklow, Phys. Rev. B **12**, 659 (1975).

[109] J. L. Lado and J. Fernández-Rossier, 2D Mater. **4**, 035002 (2017).

[110] W. Jiang, S. Li, H. Liu, G. Lu, F. Zheng, and P. Zhang, Phys. Lett. A **383**, 754 (2019).

[111] V. Kumar Gudelli and G.-Y. Guo, New J. Phys. **21**, 053012 (2019).

[112] A. K. Behera, S. Chowdhury, and S. R. Das, Appl. Phys. Lett. **114**, 232402 (2019).